LETTER | MARCH 13 2025

High-quality entangled photon source by symmetric beam displacement design

G. Paganini ; Á. Cuevas ; R. Camphausen ; A. Demuth ; V. Pruneri

APL Photonics 10, 031302 (2025)
https://doi.org/10.1063/5.0225901

High-quality entangled photon source by symmetric beam displacement design

Cite as: APL Photon. 10, 031302 (2025); doi: 10.1063/5.0225901
Submitted: 27 June 2024 • Accepted: 21 February 2025 •
Published Online: 13 March 2025

G. Paganini,[1,a)] Á. Cuevas,[1] R. Camphausen,[1] A. Demuth,[1] and V. Pruneri[1,2]

AFFILIATIONS

[1] ICFO-Institut de Ciències Fotòniques, Mediterranean Technology Park, E-08860 Castelldefels (Barcelona), Spain
[2] ICREA-Institució Catalana de Recerca i Estudis Avançats, E-08010 Barcelona, Spain

[a)] **Author to whom correspondence should be addressed:** giacomo.paganini@icfo.eu

ABSTRACT

Entangled photon sources (EPSs) are pivotal in advancing quantum communication, computing, and sensing. The demand for deploying efficient, robust EPSs in the field, characterized by exceptional (phase) stability, has become increasingly apparent. This work introduces a polarization-entangled photon source, leveraging type-0 spontaneous parametric downconversion and constructed using commercial bulk optomechanical components. Our system is versatile, enabling the generation of N00N states for sensing applications or Bell states for quantum key distribution protocols. We attained a maximal Bell inequality violation, with the average entanglement visibility exceeding 99%. The potential for further performance enhancements is also explored.

I. INTRODUCTION

Photonic entanglement is a crucial resource for modern quantum science and technology, including quantum key distribution,[1,2] teleportation,[3,4] quantum-enhanced metrology,[5,6] and quantum computing.[7,8] In all these fields, the efficient generation of high quality entangled photon pairs is essential. For instance, the advancement of next-generation projects aimed at establishing a global quantum network, through ground-to-satellite and inter-satellite connections, necessitates the development of compact, robust, and durable sources of entangled photons with high brightness and entanglement fidelity.[9]

Entangled states of light can be encoded in many degrees of freedom, such as frequency-bin,[10] energy-time,[11] time-bin,[12] orbital angular momentum,[13] and even in multiple degrees of freedom simultaneously, known as hyper-entanglement.[14] Polarization entanglement, however, has become one of the leading resources for quantum communication applications due to its relative ease of control, scalability, and compatibility with telecom infrastructure.[15] In addition, polarization-encoded quantum states have demonstrated high robustness when propagating through a turbulent atmosphere, making them the preferred choice for free-space and satellite quantum links.[9,16,17]

Various technically well-developed physical platforms enable building entangled photon sources (EPSs), both in bulk[18] and integrated photonics.[19–21] Integrated EPSs offer compactness, single mode characteristics, and especially high brightness, on the order of ~10^7 pairs/s/mW pump power in the case of PPLN waveguides.[22] However, they currently still face technical challenges that hinder their use in realistic field-deployment, particularly high outcoupling[23] losses from EPS to fiber or free-space link. In contrast, EPSs based on spontaneous parametric downconversion (SPDC) in bulk optics can provide near-ideal heralding efficiencies[18] and broad spectral and spatial multimode characteristics. They also allow access to various degrees of freedom, such as position and momentum, which, in turn, enables manipulation of structured light like OAM and vector vortex modes. These features enable hyper-entanglement capabilities[24] and multi-party quantum communications[25,26] while also facilitating higher heralding performance. Therefore, combined with the wide availability and modularity of off-the-shelf components, at present, bulk optics remain the platform of choice for EPS development.

A number of bulk optical geometries have been demonstrated to produce polarization entanglement via SPDC, including the crossed-crystal, Sagnac interferometer, and double-pass ("folded sandwich") schemes.[18]

In recent years, EPS designs similar to linear double-path interferometers have emerged. In these designs, a beam displacer (BD) splits the pump into two orthogonally and linearly polarized beams, deviating only one from the input trajectory while maintaining its original k-vector. By passing the pump beam parallel through either one[27] or two[28,29] nonlinear crystals, parallel SPDC emission can be achieved and then recombined using a second BD. This solution is easily scalable as all beams propagate in only one direction and experience less walk-off compared to the crossed-crystal scheme.

In this paper, we introduce a compact and robust scheme for polarization entanglement generation, which improves the existing beam displacer EPS designs through the novel combination of half-wave plates and Savart plates, with the latter being a composition of birefringent plates that split a beam into two parallel beams with orthogonal polarization. This innovative scheme intrinsically improves on longitudinal walk-off and compactness compared to previous studies, without compromising on the mechanical sensitivity and on the quality of the generated entanglement. Our device generates entangled photon pairs in the form of N00N states or $|\Phi^{\pm}\rangle$ Bell states, achieving near-ideal fidelity $(F = 0.992 \pm 0.001)$ and high brightness $CC = (9.50 \pm 0.03) \times 10^4$ pairs/(s · mW). It features a modular, miniaturizable architecture, making it suitable for both free-space and fiber-based quantum communication applications.

II. METHODS

A. Conceptual Design

In this work, we present a high-performance bulk-optics design for a polarization EPS, named SPaDES (Symmetric Parallel Displacement Entanglement Source). Its configuration, depicted in Fig. 1, draws inspiration from lateral displacement EPSs.[27,28,30]

A key advancement is that the longitudinal walk-off between the two parallel spatial SPDC emission modes is eliminated at every cross section along the propagation direction. This is achieved by substituting the birefringent single-beam displacement (BD) elements (used for both pump and SPDC photons) with the joint dual-beam displacement elements, referred to as balanced beam displacers (BBDs). These components can be manufactured in both integrated and fiber optics versions, but this Letter focuses on the bulk optics case. One example is the Savart plate (SP), consisting of two single-plate BDs, whose axes are rotated 90° in the transverse plane relative to each other, with no gap between the two plates. When aligned with displacement axes at ±45°, an SP splits a vertically (V) polarized single-beam state with transverse spatial coordinates (x,y), $|V\rangle|x,y\rangle$, into a two-beam state $\frac{1}{\sqrt{2}}\left(|+\rangle|x+\delta,y+\delta\rangle + e^{i\theta}|-\rangle|x-\delta,y+\delta\rangle\right)$. That is, the two parallel output beams are separated along x by a shear 2δ. Here, $|\pm\rangle \equiv \frac{1}{\sqrt{2}}(|H\rangle \pm |V\rangle)$ and $|H\rangle$ represent the horizontal polarization. Therefore, an SP functions similarly to a polarizing beam splitter (PBS) that maintains the k-vectors from input to output.[31] Referring to the scheme in Fig. 1, the pump beam (blue) has vertical polarization. The first component, SP_1, splits the beam into its $|+\rangle$ and $|-\rangle$ components. After that, a pair of half-wave plates (HWPs) rotate each component into the vertical polarization, in order to align the polarization of the state with the poling vector of the crystal, thus maximizing the SPDC generation efficiency. To increase compactness and mechanical robustness, the two HWPs are cemented together side by side with fast axes aligned at opposite inclinations with respect to the x coordinate, thus receiving the name "segmented" half-wave plate (sHWP in Fig. 1). As seen in the scheme, the state right before the ppKTP crystal is $(|V\rangle_L + |V\rangle_R)/\sqrt{2}$, where the subscripts "L" and "R" indicate the left and right paths, respectively. Each component then gets downconverted, resulting in the state $(|VV\rangle_R + |VV\rangle_L)/\sqrt{2}$. Then, $sHWP_2$ rotates the L and R components 45° in the clockwise and counterclockwise direction, respectively, obtaining the state $(|++\rangle_L + |--\rangle_R)/\sqrt{2}$. SP_2 then implements beam recombination, resulting in the output polarization-entangled state

$$|\Phi\rangle = \frac{|++\rangle + e^{i\varphi}|--\rangle}{\sqrt{2}}, \tag{1}$$

where the position Hilbert space (x,y) has been omitted, as it is global over the state representation.

The phase φ represents the optical path difference between the two parallel trajectories through our EPS. The ability to control this phase [φ in Eq. (1)] is crucial for non-locality tests, in the E91 QKD protocol. In fact, the Clauser–Horne–Shimony–Holt (CHSH) inequality can be maximally violated only if $\varphi = 0, \pi$.[32] Moreover, for the BBM91 protocol, it is necessary to measure the entangled state with high visibility in both H–V and D–A bases, and this is possible

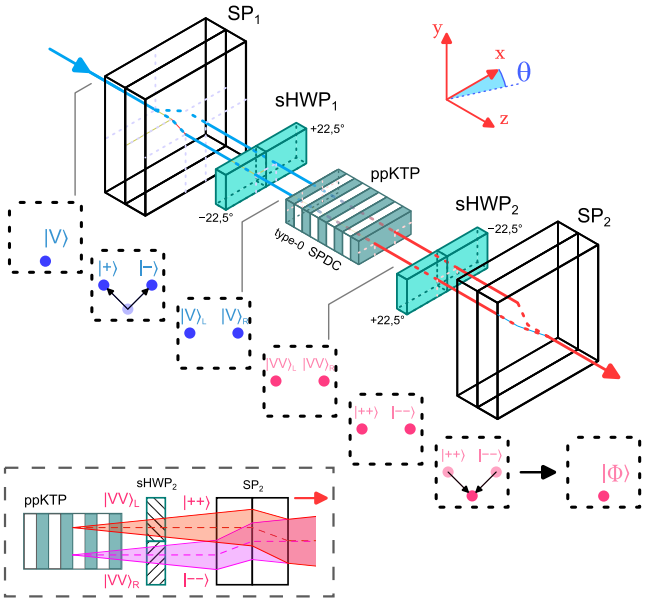

FIG. 1. SPaDES working principle. The V-polarized pump is split into $|+\rangle$ and $|-\rangle$ components by the first Savart plate SP_1. The segmented half-wave plate $sHWP_1$ rotates the polarization of both parallel modes to $|V\rangle$ [the subscript L(R) indicates the left(right) beam]. $|VV\rangle$ photon pairs are generated in the ppKTP crystal; L(R) photons are rotated to $|++\rangle(|--\rangle)$ by $sHWP_2$ and recombined by SP_2. Polarization(s) and transverse (xy) position(s) of the state after each component are shown in the boxes below. SP_2 is tilted along the xz-plane, i.e., θ, as defined in coordinate axes (top right). Inset: optical path of SPDC generation through $sHWP_2$ and SP_2.

only if φ is fully compensated.[33,34] This phase control is commonly implemented with an additional component, such as an YVO crystal (yttrium orthovanadate) or a quarter-wave plate.[15] In our design, however, we can modify φ simply through a controlled tilting of the second Savart Plate (SP_2) along the yaw axis (indicated by angle θ in Fig. 1). This tilting of SP_2 induces a difference in n_{eff} between the paths of $|++\rangle$ and $|--\rangle$, resulting in a controllable relative phase. Therefore, this enables modulating φ, granting on-demand real-time access to both the Bell states $|\Phi^{\pm}\rangle$, without the need for any additional external components. A geometrical explanation is given in Sec. III B. Note that Eq. (1) (with $\varphi = 0$) represents an $N = 2$ N00N state if the two photons are not separated into distinct spatial modes. That is, the SPaDES output can be directly used in quantum metrology schemes.[31] In contrast, here, as described in Sec. II C, we split the photons into two channels to obtain maximally entangled Bell states $|\Phi^{\pm}\rangle$.

B. Implementation

The two SPs (United Crystals) in our EPS are made of calcite and produce a nominal shear $S = 1$ mm at their respective working wavelengths ($\lambda_p = 405$ nm for SP_1; $\lambda_{s,i} = 810$ nm for SP_2). SP_1 and SP_2 lengths are $Z_{SP1} = 12.27(2)$ mm and $Z_{SP2} = 13.28(2)$ mm, respectively, and both have a 10×10 mm cross section.

The sHWPs (CeNing, calcite on the BK7 substrate) have dimensions height × width × length = $5 \times 10 \times 1$ mm^3, with fast axes at ±22.5. The interface between both sections of each sHWP was smaller than 10 μm to minimize blocking the generated beams. However, the implementation of non-collinear generation resulted in part of the SPDC cone being lost.

For the nonlinear medium, we used a type-0 periodically poled potassium titanyl phosphate (ppKTP) crystal (Raicol)[18,36] with dimensions height × width × length = $1 \times 2 \times 20$ [mm^3]. The pump laser is continuous-wave, single-frequency, centered at $\lambda_p = 405$ nm (Omicron, Bluephoton series), and was focused into the ppKTP crystal using a 200 mm lens positioned before SP_1. This configuration yielded a measured $1/e^2$ beam waist of $2w_0 = 92 \pm 2$ μm at the crystal's center. After the second Savart plate (SP_2 in Fig. 1), the pump light was subtracted via a bandpass and long-pass subsequent filters. Finally, the generated SPDC photon pairs were filtered using a 810± 5 nm bandpass filter (see Fig. 2), in order to improve photon indistinguishability and remove background, such as fluorescence, generated in the optical components.

C. Performance analysis

We demonstrated and quantified the source performance in two ways: performing two-photon interference and verifying the experimental violation of CHSH inequality.

First, we measured two-photon interference on our source's output state in order to certify the Savart plate tilting method. We projected the generated state $|\Phi\rangle$ [Eq. (1)] onto the $|H\rangle$ basis using a polarizer while varying φ in Eq. (1) by tilting SP_2. Figure 3 shows the two-photon coincidences measured at the output, demonstrating the successful transition between the states $|\Phi^+\rangle$ and $|\Phi^-\rangle$. Choosing the fitting function to be $y = A \cdot \cos(\omega x + \alpha)$, with y as the coincidences and x as the motor position, we estimated a period $T = \frac{2\pi}{\omega} = 29.85 \pm 0.03$ μm. See Appendix A for details.

Second, we quantified the generated entanglement via violation of the CHSH inequality.[32,36] As shown in Fig. 4, our CHSH characterization setup separates the entangled photon pairs, sending them to two independent measurement stations, Alice (A) and Bob (B). We used a deterministic spitting method, in which a knife-edge mirror (keM) is placed in the SPDC Fourier plane of a 200 mm lens. The momentum anti-correlation of the SPDC photon pairs here corresponds to opposite positions in the transverse plane,[18] allowing us to divide the ring-shape emission into left and right halves, which are directed to Alice and Bob, respectively. We measure coincidences between A and B, using the liquid crystal retarders (LC_A and LC_B in Fig. 4) and polarization projection setups [HWPs and polarizers (P) in Fig. 4] to obtain the Bell curves shown in Fig. 5. See Appendix B for details.

We detected a total coincidence rate $CC = (2.470 \pm 0.005) \times 10^5$ pairs/s and singles rate $SC = 2.058 \pm 0.003 \times 10^6$ counts/s, at a pump power $P = 2.6$ mW, corresponding to a brightness of $(9.50 \pm 0.03) \times 10^4$ pairs/(s · mW) and heralding efficiency $\eta = 12\%$. We therefore estimated the emitted brightness to be $\frac{CC}{\eta^2} \approx 7 \times 10^6$ pairs/(s · mW). The average fringe visibility of the fitting Bell curves (coincidences with accidentals subtracted) is $V > 0.99 \pm 0.01$. The final CHSH parameter was computed similarly to Ref. 36, obtaining $S_{\text{exp}} = 2.82 \pm 0.04$, giving a violation of the Bell inequality by 20σ.

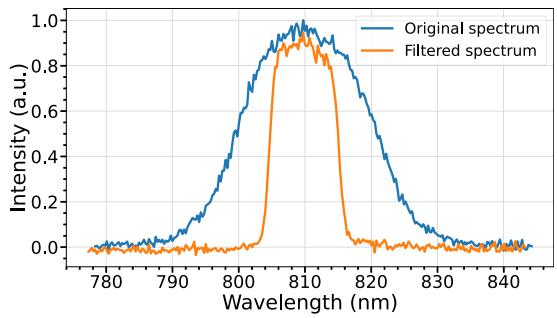

FIG. 2. Emission spectrum. Generated SPDC spectrum (blue), with $\Delta\lambda = 22$ nm (FWHM), and filtered spectrum (orange), with $\Delta\lambda = 10$ nm (FWHM).

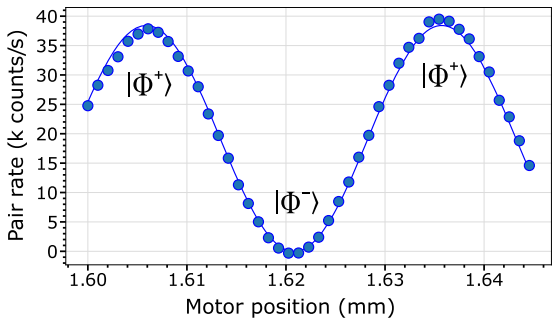

FIG. 3. Varying entangled state by Savart plate tilting. Two-photon coincidences vs stepper motor position; φ in Eq. (1) is modulated using a motor tilting SP_2. Blue circles: measured coincidences; solid line: cosine fitting function.

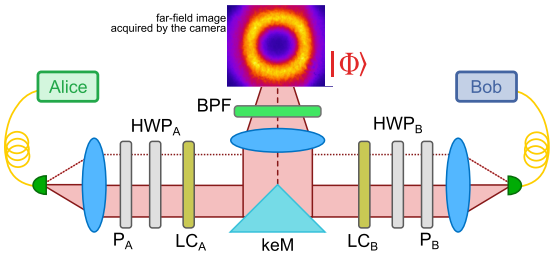

FIG. 4. CHSH setup. The far-field plane of the SPDC beam splits in half with a knife-edge mirror (keM). Due to SPDC momentum anti-correlation, photon pairs are deterministically divided between Alice (A) and Bob (B) arms.

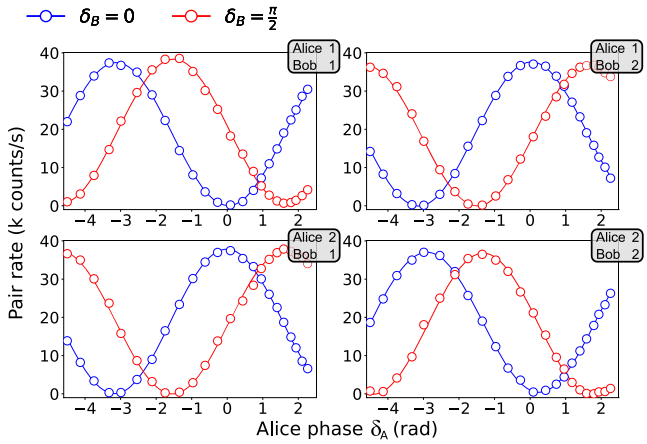

FIG. 5. CHSH results. Coincidences between A and B, varying Alice phase δ_A for fixed Bob phase $\delta_B = 0, \frac{\pi}{2}$. Measurement settings 1(2) (gray boxes) correspond to horizontal(vertical) detected polarization. Circles: measured coincidences (Poissonian standard error smaller than marker size); solid lines: fitting functions.

From such S_{exp}, we then obtain the Bell state visibility, using the expression $S_{exp} = \mathscr{V}_S \cdot 2\sqrt{2}$. Assuming a mixed-state Werner representation $\rho = \mathscr{V}_S|\Phi\rangle\langle\Phi| + \frac{1-\mathscr{V}_S}{4}\mathbb{I}\otimes\mathbb{I}$ as the worst possible scenario, the two-qubit fidelity corresponds to that in Ref. 37,

$$F = \frac{1}{4}\left(\frac{3}{2}\sqrt{\mathscr{V}_S} + \frac{1}{2}\sqrt{4-3\mathscr{V}_S}\right)^2. \quad (2)$$

We therefore estimate a lower bound fidelity $F = 0.992 \pm 0.001$, with the error given by Gaussian propagation.

A brief overview of the source performance is displayed in Table I.

TABLE I. EPS measured performance. *CC*: coincidence brightness adjusted for detection efficiency (CHSH inequality measurement), $\eta = CC/SC$: heralding efficiency, and CAR: coincidences to accidentals rate.

Specification	Mean value
CC (1/(s · mW))	9.5×10^4
Heralding η	12%
CAR	14
Visibility	99%
Fidelity (lower bound)	0.99
CHSH parameter *S*	2.82 ± 0.04

III. COMPACT EPS ADVANTAGES

A. SPaDES architecture vs state-of-the-art

The state-of-the-art for polarization-entangled photon sources is represented by the Sagnac architecture, which many papers have reported to deliver excellent results.[15,18,38] The Sagnac EPS offers a phase-stable platform, however, at the expense of wavelength-dependent performance (polarization extinction, polarization rotation, reflectivity, etc.) due to the necessity for dual-wavelength components. In addition, the experimentally challenging alignment and the high precision required when positioning the crystal at the center of the loop drastically hinder the scalability of this design for field applications. Moreover, slight misalignment of the crystal position can modify differently the counter-propagating SPDC generations, thus increasing both longitudinal and lateral crosstalk between photons.[39]

Linear beam displacer based sources[27,28,30] propose to solve these problems, with simple, robust, and compact architectures. SPaDES represents an evolution of these schemes, aiming to further simplify the design and improve mechanical sensitivity and miniaturizability. Compared to Ref. 28, our design uses only a single nonlinear crystal, rather than two. Thereby, SPaDES avoids potential related issues stemming from the use of two distinct crystals, such as phase-matching temperature differences and spectral distinguishability of the two SPDC generations. SPaDES also replaces the BD pairs with monolithic Savart plates, which improves stability and compactness and enables facile accurate modulation of φ in Eq. (1) (see Appendix A). Compared to single BD schemes,[27,30] our design completely removes longitudinal walk-off between the two polarization paths at all points in the source. This enables implementations with arbitrarily short nonlinear crystals and in the strong pump focusing regime. See Sec. IV for further details.

B. Longitudinal walk-off

The SPaDES design eliminates all walk-off, i.e., the two SPDC generation modes focus in the exact same longitudinal position in the nonlinear crystal. In order to demonstrate the impact of single beam displacers, beam displacer sources design the generation, superposition, and collection of entangled photons; we reproduced the case in which a focused beam passes through a BD element, as displayed in Fig. 6(a). We measured the relative longitudinal locations of the two beam waists after the BD. We performed the measurement at $\lambda = 405$ nm for a BD with a lateral shear $S_{BD} = 1.010 \pm 0.001$ mm and for a Savart plate with $S_{SP} = 0.972 \pm 0.001$ mm. The light source was initially collimated to a diameter $D = 1.4$ mm and focused down to $2w_0 \sim 20$ μm using a $f_1 = 150$ mm lens.

The beam displacer and Savart plate were placed in the middle point between the f_1 lens and w_0, simulating the EPS configuration. We detected the beam profile using a CMOS camera, which was longitudinally translated along the optical *z* axis

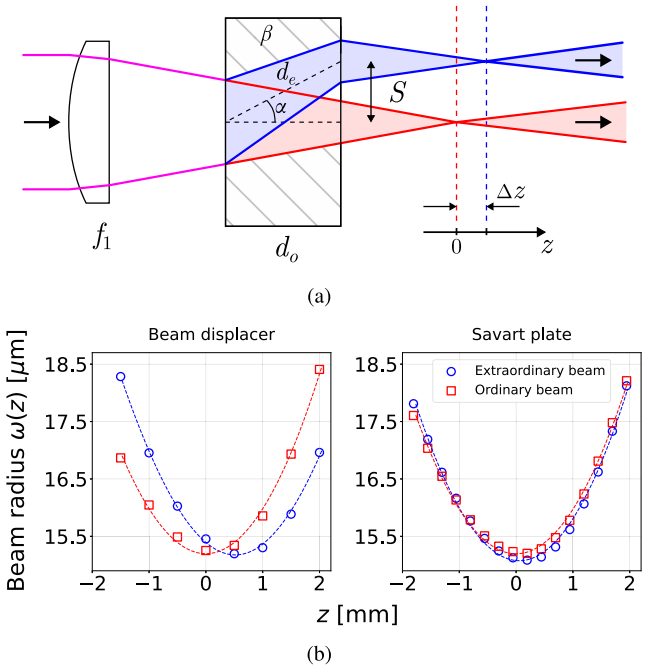

FIG. 6. (a) Diagram of longitudinal walk-off in a BD element using a beam focused using a f_1 = 150 mm lens. Vertical segmented lines at the valleys of the hyperbolas indicating the associated value. (b) Results for the respective beam waist positions.

by means of a motorized stage, in order to capture the different focusing planes. The measured beam waists in each z position are reported in Fig. 6(b) for both the single beam displacer and the Savart plate.

For the BD element with d_o = 8.73 mm, the expected walk-off is Δz_{BD} = 0.542 mm (see Appendix C). The experimental result, extrapolated from the fitting functions in Fig. 6(b), is $\Delta\tilde{z}_{BD}$ = 0.52 ± 0.03 mm. For the Savart plate, we obtained a walk-off $\Delta\tilde{z}_{SP}$ = 0.06 ± 0.03 mm. We see that $\Delta\tilde{z}_{BD}$ is at least one order of magnitude higher than standard crystal periodicities, making the BD an unsuitable component when utilizing chirped poling periods. This also limits the minimum length of the crystal one can employ: for ~1 mm long crystals, by placing the waist of one polarization in the center of it, we already would find the waist of the orthogonal component outside the crystal. The Savart plate walk-off did not appear to be perfectly null due to experimental error. In addition, some minor astigmatism typical of these components could have affected the accuracy of this measurement.

IV. DISCUSSION

The estimated brightness of our source was $CC = (9.50 \pm 0.03) \times 10^4$ pairs/(s · mW), which is sufficient for achieving optimal secure key rates in realistic free-space or fiber entanglement-based QKD applications.[40] Our source brightness (Table I) is, however, lower than the maximum reported values in the literature.[15] We attribute this mainly to the choice of an SPDC working-point in the non-collinear phase-matching regime, which induces a lower spectral brightness compared to the collinear case.[41] Nonetheless, the advantage of the non-collinear regime is that it enables deterministically splitting the generated photon pairs, without relying on non-degenerate spectral correlations, as would be required when using a sharp dichroic mirror or wavelength-division multiplexing devices.

Optical losses in our EPS are attributed to the optical components' transmissivities (78%) and fiber coupling. In particular, $sHWP_2$, at the interface between the two segmented-HWP segments (see the inset of Fig. 1), partially absorbs a portion of each SPDC far-field ring (~10%). Moreover, the knife-edge mirror (keM in Fig. 4), due to fabrication limits, induces some diffraction and scattering effects that cause additional losses (~15%) to light in proximity of the edge.

As mentioned in Sec. III A, the SPaDES design presents some advantages compared to other linear beam displacer sources in the literature.[27,28,30] For example, our source is more suitable for wave-division multiplexing (WDM) and quantum communication applications, such as increasing network capacity[25] or boosting the secure key-rate.[42] This is because WDM-based schemes require entangled photon emission across a broad wavelength range, with high spectral indistinguishability across the entire range between the two SPDC generations. This broad indistinguishability requirement is challenging to meet for any double crystal EPS,[28] as, in general, two distinct nonlinear crystals will have non-identical emission spectra.[43] In contrast, the single-crystal SPaDES intrinsically avoids this issue. Compared to Refs. 27 and 30, the SPaDES' zero longitudinal walk-off allows, first, using shorter nonlinear crystals that yield a broader spectrum, and second, tighter pump focusing, which maximizes fiber-coupled pair rates across a wide wavelength range.[33] As another application example, its compatibility with short crystals allows SPaDES to generate entangled photons with strong spatial correlations, which are a requirement in many quantum imaging schemes.[31,44] Finally, superior mechanical characteristics of SPaDES will enable its use in harsh environments, such as for satellite-based use cases. Compared to Ref. 28, monolithic Savart plates provide better stability and avoid potential issues of refraction, back-reflection, and astigmatism caused by the gap between separate BDs. Moreover, the use of a single nonlinear crystal allows greater miniaturization in the transverse plane, due to the lack of physical interface between the two SPDC generation zones. Due to this, the separation can be lowered; hence, the SP can be shortened. At the same time, by eliminating the walk-off, the crystal can also be shortened in the longitudinal plane, provided appropriate focusing. A tight focus will then allow for lower separation between the beams and reinforce the advantage of a zero-walk-off fully-symmetric design. We emphasize that SPaDES miniaturization involves trade-offs, such as in the generation spectrum and efficiency. Therefore, systematic design choices are required to optimize parameters for a given use case.

In addition to integrating the above listed advantages, the SPaDES design has mechanical phase stability at least equal to single-BD designs,[27,30] as confirmed by our measurements (see the supplementary material 1), similar to Refs. 45 and 46.

We note that, when seeking compactness and high scalability, it is natural to mention integrated platforms, which offer some advantages over traditional bulk sources. In particular, waveguide-based sources excel in brightness due to their intense light confinement.

These can be specifically engineered to produce light with desirable single-mode characteristics (spatially and spectrally).[19,47] Photonic Integrated Circuits (PICs) mark a significant advancement for vertically integrating quantum technologies,[21,48] given their scalable manufacturing processes. However, at present, the versatility and modularity of such PIC systems are limited, as they cannot harness multi-modal characteristics such as position, momentum, and orbital angular momentum correlations. In addition, integration is feasible only for narrowband, single-mode systems, and efficiently outcoupling from PIC EPSs to free-space or fiber remains challenging.[18] Finally, a promising candidate for the next generation of quantum technologies is semiconductor-based quantum dots that provide on-demand entangled photon pairs with narrow linewidth and negligible multiphoton events.[20,49] However, quantum dot sources have not yet attained the performance levels of their bulk EPS counterparts, both in terms of brightness and in state fidelity,[20,50,51] and typically require cryogenic temperatures that limit field deployment and scalability.

V. CONCLUSION

In this work, we have shown a SPDC-based polarization entangled photon pair source (EPS) design, based on the evolution of previous linear beam-displacer architectures. This design is based on laterally displacing the $|+\rangle$ and $|-\rangle$ components of a vertically polarized pump beam and sending these parallel modes through the nonlinear crystal. The two generated SPDC modes are then recombined to obtain the Bell state $|\Phi\rangle = \frac{|++\rangle+e^{i\varphi}|--\rangle}{\sqrt{2}}$. The parallel splitting of the pump and recombination of the SPDC modes are performed by a pair of Savart plates, which symmetrically displace each polarization mode. This evolution serves the purpose to completely remove the longitudinal walk-off from inside the crystal.

Our EPS generates polarization entangled photons in the form of N00N states or Bell states, easily tunable between the $|\Phi^+\rangle$ and $|\Phi^-\rangle$ states through motorized tilting of the second Savart plates. Characterizing the entanglement generated by our source, we measured a CHSH parameter $S = 2.82 \pm 0.04$ ($\sim 20\sigma$ violation of the CHSH inequality), which implies a near-ideal fidelity $F = 0.992 \pm 0.001$, from Ref. 37. The brightness of our EPS was measured to be $CC = (9.50 \pm 0.03) \times 10^4$ pairs/(s · mW), which gives an estimated entangled photon pair emission rate $CC_{\mathrm{em}} = 105 \times 10^6$ pairs/(s · mW) when taking into account system losses. We also studied the mechanical robustness and longitudinal walk-off of our EPS. In comparison with existing standard BD designs, we found that our source drastically reduces longitudinal walk-off while maintaining near-identical mechanical stability.

Our design combines a series of unique ideas, whose implementation offers high performance either for (i) scalability: all components can be easily miniaturized both in the longitudinal and transverse dimensions, thanks to the virtually null walk-off and the use of a single nonlinear crystal, or for (ii) harsh environments: bulk optics offers one of the best generation stabilities under thermal/pressure fluctuations, making our EPS an ideal candidate for space quantum communications.

Future upgrades will include superior segmented half-wave plates in order to improve the heralding efficiency, as well as development of an engineering model to further miniaturize the setup and enable real-environment qualification, such as space qualification.

SUPPLEMENTARY MATERIAL

The supplementary material evaluates the mechanical robustness of the SPaDES design compared to beam displacers (BDs). It analyzes phase response sensitivity to tilting misalignments by measuring interference patterns shifts as a function of SP and BD tilt angles.[31] The results confirm that SPaDES maintains alignment robustness comparable to BD-based designs, supporting its feasibility for quantum applications.

ACKNOWLEDGMENTS

This study was supported by MCIN with funding from the European Union Next Generation EU (Grant No. PRTR-C17.I1) and by the Generalitat de Catalunya. This project has received funding from the European Union's Horizon Europe research and innovation program under the project "Quantum Security Networks Partnership" (QSNP, Grant Agreement No 101114043). This work was partially funded by Grant No. CEX2019-000910-S [MCIN/AEI/10.13039/501100011033], Fundació Cellex, Fundació Mir-Puig, and Generalitat de Catalunya through CERCA. G.P. acknowledges funding from the European Union's Horizon Europe research and innovation program under the Marie Skłodowska-Curie Grant Agreement No. 101081441. A.C. work was funded by Grant No. CEX2019-000910-S [MCIN/AEI/10.13039/501100011033], Fundació Cellex, Fundació Mir-Puig, and Generalitat de Catalunya through CERCA. R.C. acknowledges funding from the European Union's Horizon Europe research and innovation program under the Marie Sklodowska-Curie Grant Agreement No. 713729 (ICFOstepstone 2) and from the European Union's Horizon Europe research and innovation program under Grant Agreement No. 101082596 (QUDICE). A.D. acknowledges support of the ICFO CELLEX PhD-fellowship.

AUTHOR DECLARATIONS

Conflict of Interest

A.C., R.C., A.D., and V.P. are co-inventors of a patent application related to the content of this paper.

Author Contributions

G. Paganini: Conceptualization (supporting); Data curation (lead); Formal analysis (lead); Investigation (lead); Methodology (equal); Software (lead); Validation (equal); Visualization (equal); Writing – original draft (lead); Writing – review & editing (equal). **A. Cuevas**: Conceptualization (equal); Data curation (equal); Formal analysis (equal); Investigation (equal); Project administration (equal); Supervision (equal); Visualization (equal); Writing – original draft (equal); Writing – review & editing (equal). **R. Camphausen**: Conceptualization (equal); Methodology (equal); Project administration (equal); Supervision (equal); Visualization (equal); Writing – original draft

(equal); Writing – review & editing (equal). **A. Demuth**: Conceptualization (equal); Methodology (equal); Project administration (equal); Visualization (equal); Writing – original draft (equal); Writing – review & editing (equal). **V. Pruneri**: Conceptualization (equal); Funding acquisition (lead); Project administration (equal); Supervision (equal); Writing – review & editing (equal).

DATA AVAILABILITY

The data that support the findings of this study are available from the corresponding author upon reasonable request.

APPENDIX A: SAVART-PLATE TILTING PHASE-SHIFTING

To demonstrate that tilting the Savart plate SP_2 allows tuning φ in Eq. (1), we project the generated state $|\Phi^+\rangle$ onto H using a polarizer. This output is single-mode fiber (SMF) coupled, and the pairs are split probabilistically with a 50–50 fiber beam splitter (FBS, Thorlabs). We measure two-photon coincidences between the FBS outputs a and b, using a pair of single-photon avalanche diode (SPAD) detectors, extracting coincidences using a 1 ns window, and subtracting accidentals. These coincidences depend on φ in Eq. (1) as

$$P_{a,b} \equiv |\langle H_a, H_b|\Phi\rangle_{\mathrm{FBS}}|^2 = \frac{1 + \mathscr{V}_{\mathrm{SP}} \cos(\varphi)}{4}, \tag{A1}$$

where we have introduced the interference visibility (V_{SP}). This coincidence curve is shown in Fig. 3, where we vary the tilting angle θ of SP_2 with respect to the optical axis (see Fig. 1).

SP_2 tilting is implemented using a stepper motor pushing one side of SP_2 along the z axis. The motor is mounted on the side of the Savart plate holder to control its tilt angle θ in the yaw direction (see Fig. 1), where motor position $p \propto \sin\theta$ and $\sin\theta \approx \theta$ for $\theta \approx 0$. Yaw angle θ is proportional to the phase between the $|+\rangle$ and $|-\rangle$ polarization modes.[45] Therefore, the stepper motor position is directly proportional to φ in Eq. (1). By fitting a cosine function to the two-photon interference curve (Fig. 3), we extract the motor position values corresponding to desired phases $\varphi = 0, \pi$, in order to switch between $|\Phi^\pm\rangle$ states.

The coincidence interference visibilities with and without accidentals subtraction were $\mathscr{V}_{SP} = 1.000 \pm 0.010$ and $\widetilde{\mathscr{V}}_{\mathrm{sp}} = 0.840 \pm 0.008$, respectively. This result also shows that SMF-coupling remains unaffected by the Savart plate tilting.

APPENDIX B: CHSH INEQUALITY

As shown in Fig. 4, Alice (Bob) side contains a liquid crystal LC_A (LC_B) placed at 45° rotation to implement φ_A (φ_B) phase between vertical and horizontal polarizations. Note that, before the beam splitting via the knife-edge mirror, the state in Eq. (1) is rotated with a HWP to $\frac{|HH\rangle + e^{i\varphi}|VV\rangle}{\sqrt{2}}$.

The half-wave plates (HWP_A and HWP_B) and polarizers (P_A and P_B) in each arm enable the projection into vertical and horizontal polarizations. By alternating between these polarization states, we can measure coincidences across various polarization combinations without needing the four detectors typically required in Aspect-type experiments.[36] This is achieved by simply rotating the polarization of the state. The light in A and B is coupled into SMFs and sent to SPADs for coincidence detection (1 ns window), with accidentals removed. The optimal Bell angles for Bob are $\frac{\pi}{2}$ apart.[52] Therefore, the liquid crystal LC_B in Fig. 4 was fixed to $\delta_B = 0, \frac{\pi}{2}$, while LC_A was scanned over an entire period, in order to find the δ_A values that maximize the inequality. For each Bob phase setting ($\delta_B = 0, \frac{\pi}{2}$), we obtained four coincidence curves for four combinations of the four channels Alice 1,2 and Bob 1,2. Here, Alice 1(2) and Bob 1(2) correspond to horizontal(vertical) detected polarization. These results are shown in Fig. 5.

APPENDIX C: LONGITUDINAL WALK-OFF MEASUREMENT

As shown in the optical scheme of Fig. 6(a), the extraordinary beam path corresponds to $d_e = \sqrt{d_o^2 + S^2}$, with d_o as the ordinary beam path that also coincides with the BD width. The optical path difference can be calculated as

$$\Delta z = d_o n_o - d_e n_e, \tag{C1}$$

where

$$n = 1/\sqrt{\frac{\cos^2(\alpha-\beta)}{n_o^2} + \frac{\sin^2(\alpha-\beta)}{n_e^2}} \tag{C2}$$

is the effective refractive index for the non-ordinary polarized light. Here, $\alpha = \arctan(S/d_o)$ is the deviation angle and β the optical axis angle. The refractive indices of the calcite for ordinary (extraordinary) polarized light are $n_o = 1.66$ ($n_e = 1.49$). The BD was manufactured with $\beta = 45°$ and thickness $Z_{\mathrm{BD}} = 8.73$ mm; therefore, we predict $\Delta z = 0.542$ mm.

REFERENCES

[1] N. Gisin, G. Ribordy, W. Tittel, and H. Zbinden, "Quantum cryptography," Rev. Mod. Phys. **74**, 145–195 (2002).
[2] H. J. Kimble, "The quantum internet," Nature **453**, 1023–1030 (2008).
[3] C. H. Bennett, G. Brassard, C. Crépeau, R. Jozsa, A. Peres, and W. K. Wootters, Phys. Rev. Lett. **70**, 1895–1899 (1993).
[4] D. Bouwmeester, J.-W. Pan, K. Mattle, M. Eibl, H. Weinfurter, and A. Zeilinger, Nature **390**, 575–579 (1997).
[5] C. L. Degen, F. Reinhard, and P. Cappellaro, "Quantum sensing," Rev. Mod. Phys. **89**, 035002 (2017).
[6] M. Gilaberte Basset, F. Setzpfandt, F. Steinlechner, E. Beckert, T. Pertsch, and M. Gräfe, "Perspectives for applications of quantum imaging," Laser Photonics Rev. **13**, 1900097 (2019).
[7] S. Slussarenko and G. J. Pryde, "Photonic quantum information processing: A concise review," Appl. Phys. Rev. **6**, 041303 (2019).
[8] L. S. Madsen, F. Laudenbach, M. F. Askarani, F. Rortais, T. Vincent, J. F. F. Bulmer, F. M. Miatto, L. Neuhaus, L. G. Helt, M. J. Collins, A. E. Lita, T. Gerrits, S. W. Nam, V. D. Vaidya, M. Menotti, I. Dhand, Z. Vernon, N. Quesada, and J. Lavoie, "Quantum computational advantage with a programmable photonic processor," Nature **606**, 75–81 (2022).
[9] C.-Y. Lu, Y. Cao, C.-Z. Peng, and J.-W. Pan, "Micius quantum experiments in space," Rev. Mod. Phys. **94**, 035001 (2022).
[10] C. Bernhard, B. Bessire, T. Feurer, and A. Stefanov, "Shaping frequency-entangled qudits," Phys. Rev. A **88**, 032322 (2013).
[11] A. Cuevas, G. Carvacho, G. Saavedra, J. Cariñe, W. a. T. Nogueira, M. Figueroa, A. Cabello, P. Mataloni, G. Lima, and G. B. Xavier, "Long-distance distribution of genuine energy-time entanglement," Nat. Commun. **4**, 2871 (2013).

[12]L. Ma, O. Slattery, T. Chang, and X. Tang, "Non-degenerated sequential time-bin entanglement generation using periodically poled KTP waveguide," Opt. Express **17**, 15799–15807 (2009).
[13]H. Cao, S.-C. Gao, C. Zhang, J. Wang, D.-Y. He, B.-H. Liu, Z.-W. Zhou, Y.-J. Chen, Z.-H. Li, S.-Y. Yu, J. Romero, Y.-F. Huang, C.-F. Li, and G.-C. Guo, "Distribution of high-dimensional orbital angular momentum entanglement over a 1 km few-mode fiber," Optica **7**, 232–237 (2020).
[14]P. Zhao, M.-Y. Yang, S. Zhu, L. Zhou, W. Zhong, M.-M. Du, and Y.-B. Sheng, "Generation of hyperentangled state encoded in three degrees of freedom," Sci. China Phys., Mech. Astron. **66**, 100311 (2023).
[15]E. Brambila, R. Gómez, R. Fazili, M. Gräfe, and F. Steinlechner, "Ultrabright polarization-entangled photon pair source for frequency-multiplexed quantum communication in free-space," Opt. Express **31**, 16107–16117 (2023).
[16]M. Aspelmeyer, H. R. Bohm, T. Gyatso, T. Jennewein, R. Kaltenbaek, M. Lindenthal, G. Molina-Terriza, A. Poppe, K. Resch, M. Taraba, R. Ursin, P. Walther, and A. Zeilinger, "Long-distance free-space distribution of quantum entanglement," Science **301**, 621–623 (2003).
[17]J. Yin, Y.-H. Li, S.-K. Liao, M. Yang, Y. Cao, L. Zhang, J.-G. Ren, W.-Q. Cai, W.-Y. Liu, S.-L. Li, R. Shu, Y.-M. Huang, L. Deng, L. Li, Q. Zhang, N.-L. Liu, Y.-A. Chen, C.-Y. Lu, X.-B. Wang, F. Xu, J.-Y. Wang, C.-Z. Peng, A. K. Ekert, and J.-W. Pan, "Entanglement-based secure quantum cryptography over 1,120 kilometres," Nature **582**, 501–505 (2020).
[18]A. Anwar, C. Perumangatt, F. Steinlechner, T. Jennewein, and A. Ling, "Entangled photon-pair sources based on three-wave mixing in bulk crystals," Rev. Sci. Instrum. **92**, 041101 (2021).
[19]T. Suhara, "Generation of quantum-entangled twin photons by waveguide nonlinear-optic devices," Laser Photonics Rev. **3**, 370–393 (2009).
[20]C. Schimpf, M. Reindl, F. Basso Basset, K. D. Jöns, R. Trotta, and A. Rastelli, "Quantum dots as potential sources of strongly entangled photons: Perspectives and challenges for applications in quantum networks," Appl. Phys. Lett. **118**, 100502 (2021).
[21]A. Politi, M. J. Cryan, J. G. Rarity, S. Yu, and J. L. O'Brien, "Silica-on-silicon waveguide quantum circuits," Science **320**, 646–649 (2008).
[22]P. S. Kuo, V. B. Verma, and S. Woo Nam, "Demonstration of a polarization-entangled photon-pair source based on phase-modulated PPLN," OSA Continuum **3**, 295–304 (2020).
[23]H. Mahmudlu, R. Johanning, A. van Rees, A. Khodadad Kashi, J. P. Epping, R. Haldar, K.-J. Boller, and M. Kues, "Fully on-chip photonic turnkey quantum source for entangled qubit/qudit state generation," Nat. Photonics **17**, 518–524 (2023).
[24]L. Achatz, L. Bulla, S. Ecker, E. A. Ortega, M. Bartokos, J. C. Alvarado-Zacarias, R. Amezcua-Correa, M. Bohmann, R. Ursin, and M. Huber, "Simultaneous transmission of hyper-entanglement in three degrees of freedom through a multicore fiber," npj Quantum Inf. **9**, 45 (2023).
[25]S. Wengerowsky, S. K. Joshi, F. Steinlechner, H. Hübel, and R. Ursin, "An entanglement-based wavelength-multiplexed quantum communication network," Nature **564**, 225–228 (2018).
[26]E. A. Ortega, K. Dovzhik, J. Fuenzalida, S. Wengerowsky, J. C. Alvarado-Zacarias, R. F. Shiozaki, R. Amezcua-Correa, M. Bohmann, and R. Ursin, "Experimental space-division multiplexed polarization-entanglement distribution through 12 paths of a multicore fiber," PRX Quantum **2**, 040356 (2021).
[27]A. Lohrmann, C. Perumangatt, A. Villar, and A. Ling, "Broadband pumped polarization entangled photon-pair source in a linear beam displacement interferometer," Appl. Phys. Lett. **116**, 021101 (2020).
[28]R. Horn and T. Jennewein, "Auto-balancing and robust interferometer designs for polarization entangled photon sources," Opt. Express **27**, 17369–17376 (2019).
[29]R. Fazili, P. S. Chauhan, U. Chandrashekara, A. Kržič, R. Gómez, M. Gräfe, and F. Steinlechner, "Simple but efficient polarization-entangled photon sources," J. Opt. Soc. Am. B **41**, 2692–2701 (2024).
[30]C. Perumangatt, A. Lohrmann, and A. Ling, "Experimental conversion of position correlation into polarization entanglement," Phys. Rev. A **102**, 012404 (2020).
[31]R. Camphausen, Á. Cuevas, L. Duempelmann, R. A. Terborg, E. Wajs, S. Tisa, A. Ruggeri, I. Cusini, F. Steinlechner, and V. Pruneri, "A quantum-enhanced wide-field phase imager," Sci. Adv. **7**, eabj2155 (2021).
[32]J. F. Clauser, M. A. Horne, A. Shimony, and R. A. Holt, "Proposed experiment to test local hidden-variable theories," Phys. Rev. Lett. **23**, 880–884 (1969).
[33]F. Steinlechner and V. Pruneri, "Sources of photonic entanglement for applications in space," Ph.D. thesis, Universitat Politècnica de Catalunya, 2015.
[34]S. Wengerowsky and A. Zeilinger, "Two-photon polarization-entanglement for experiments and applications in quantum communications," Ph.D. thesis, Universität Wien, 2021.
[35]M. Fiorentino and R. G. Beausoleil, "Compact sources of polarization-entangled photons," Opt. Express **16**, 20149–20156 (2008).
[36]A. Aspect, "Proposed experiment to test the nonseparability of quantum mechanics," Phys. Rev. D **14**, 1944–1951 (1976).
[37]E. Riedel Gårding, N. Schwaller, C. L. Chan, S. Y. Chang, S. Bosch, F. Gessler, W. R. Laborde, J. N. Hernandez, X. Si, M.-A. Dupertuis, and N. Macris, "Bell diagonal and Werner state generation: Entanglement, non-locality, steering and discord on the IBM quantum computer," Entropy **23**, 797 (2021).
[38]T. Kim, M. Fiorentino, and F. N. C. Wong, "Phase-stable source of polarization-entangled photons using a polarization Sagnac interferometer," Phys. Rev. A **73**, 012316 (2006).
[39]E. Beckert, O. de Vries, R. Ursin, F.-O. Steinlechner, M. Gräfe, and M. G. Basset, "A space-suitable, high brilliant entangled photon source for satellite based quantum key distribution," SPIE Proc. **10910**, 260–273 (2019).
[40]S. Ecker, B. Liu, J. Handsteiner, M. Fink, D. Rauch, F. Steinlechner, T. Scheidl, A. Zeilinger, and R. Ursin, "Strategies for achieving high key rates in satellite-based QKD," npj Quantum Inf. **7**, 5 (2021).
[41]F. Steinlechner, M. Gilaberte, M. Jofre, T. Scheidl, J. P. Torres, V. Pruneri, and R. Ursin, "Efficient heralding of polarization-entangled photons from type-0 and type-II spontaneous parametric downconversion in periodically poled $KTiOPO_4$," J. Opt. Soc. Am. B **31**, 2068 (2014).
[42]J. Pseiner, L. Achatz, L. Bulla, M. Bohmann, and R. Ursin, "Experimental wavelength-multiplexed entanglement-based quantum cryptography," Quantum Sci. Technol. **6**, 035013 (2021).
[43]F. Steinlechner, P. Trojek, M. Jofre, H. Weier, D. Perez, T. Jennewein, R. Ursin, J. Rarity, M. W. Mitchell, J. P. Torres, H. Weinfurter, and V. Pruneri, "A high-brightness source of polarization-entangled photons optimized for applications in free space," Opt. Express **20**, 9640 (2012).
[44]P. Cameron, B. Courme, C. Vernière, R. Pandya, D. Faccio, and H. Defienne, "Adaptive optical imaging with entangled photons," Science **383**, 1142–1148 (2024).
[45]C. Zhang, J. Zhao, and Y. Sun, "Influences of the thickness, misalignment, and dispersion of the Savart polariscope on the optical path difference and spectral resolution in the polarization interference imaging spectrometer," Appl. Opt. **50**, 3497–3504 (2011).
[46]C. Zhang, B. Xiangli, B. Zhao, and X. Yuan, "A static polarization imaging spectrometer based on a Savart polariscope," Opt. Commun. **203**, 21–26 (2002).
[47]E. Pomarico, B. Sanguinetti, N. Gisin, R. Thew, H. Zbinden, G. Schreiber, A. Thomas, and W. Sohler, "Waveguide-based OPO source of entangled photon pairs," New J. Phys. **11**, 113042 (2009).
[48]J. Mower and D. Englund, "Efficient generation of single and entangled photons on a silicon photonic integrated chip," Phys. Rev. A **84**, 052326 (2011).
[49]D. A. Vajner, L. Rickert, T. Gao, K. Kaymazlar, and T. Heindel, "Quantum communication using semiconductor quantum dots," Adv. Quantum Technol. **5**, 2100116 (2022).
[50]A. J. Hudson, R. M. Stevenson, A. J. Bennett, R. J. Young, C. A. Nicoll, P. Atkinson, K. Cooper, D. A. Ritchie, and A. J. Shields, "Coherence of an entangled exciton-photon state," Phys. Rev. Lett. **99**, 266802 (2007).
[51]D. Huber, M. Reindl, J. Aberl, A. Rastelli, and R. Trotta, "Semiconductor quantum dots as an ideal source of polarization-entangled photon pairs on-demand: A review," J. Opt. **20**, 073002 (2018).
[52]J. S. Bell, "On the Einstein Podolsky Rosen paradox," Phys. Phys. Fiz. **1**, 195–200 (1964).